Engineering 18 (2022) 154–160

Contents lists available at ScienceDirect

Engineering

journal homepage: www.elsevier.com/locate/eng

Research
Material Science and Engineering—Article

# Atomic Interface Catalytically Synthesizing SnP/CoP Hetero-Nanocrystals within Dual-Carbon Hybrids for Ultrafast Lithium-Ion Batteries

Chen Hu [a], Yanjie Hu [a], Aiping Chen [a], Xuezhi Duan [b], Hao Jiang [a,*], Chunzhong Li [a,b,*]

[a] Key Laboratory for Ultrafine Materials of Ministry of Education, Frontiers Science Center for Materiobiology and Dynamic Chemistry, School of Materials Science and Engineering, East China University of Science and Technology, Shanghai 200237, China
[b] Shanghai Engineering Research Center of Hierarchical Nanomaterials, School of Chemical Engineering, East China University of Science and Technology, Shanghai 200237, China

ARTICLE INFO

*Article history:*
Received 1 December 2020
Revised 14 November 2021
Accepted 19 November 2021
Available online 31 May 2022

*Keywords:*
Catalytic phosphorization
SnP
Hetero-nanocrystals
Fast charging
Li-ion batteries

ABSTRACT

Tin phosphides are attractive anode materials for ultrafast lithium-ion batteries (LIBs) because of their ultrahigh Li-ion diffusion capability and large theoretical-specific capacity. However, difficulties in synthesis and large size enabling electrochemical irreversibility impede their applications. Herein, an *in situ* catalytic phosphorization strategy is developed to synthesize SnP/CoP hetero-nanocrystals within reduced graphene oxide (rGO)-coated carbon frameworks, in which the SnP relative formation energy is significantly decreased according to density functional theory (DFT) calculations. The optimized hybrids exhibit ultrafast charge/discharge capability (260 $mA{\cdot}h{\cdot}g^{-1}$ at 50 $A{\cdot}g^{-1}$) without capacity fading (645 $mA{\cdot}h{\cdot}g^{-1}$ at 2 $A{\cdot}g^{-1}$) through 1500 cycles. The lithiation/delithiation mechanism is disclosed, showing that the 4.0 nm sized SnP/CoP nanocrystals possess a very high reversibility and that the previously formed metallic Co of CoP at a relatively high potential accelerates the subsequent reaction kinetics of SnP, hence endowing them with ultrafast charge/discharge capability, which is further verified by the relative dynamic current density distributions according to the finite element analysis.



## 1. Introduction

Ultrafast lithium-ion batteries (LIBs) are believed to significantly trigger the extensive applications of pure electric buses, taxis, 24 h mobile tools, and so forth [1–3]. The pivotal goal is to exploit practicable anode materials that demand rapid $Li^+$ insertion/extraction and high reversibility because this process easily causes severe structural damage and abundant "dead" $Li^+$ [4,5]. The rapid charge/discharge performance is chiefly related to the $Li^+$ diffusion coefficient ($D_{Li^+}$) [6,7]. The value is about $10^{-6}$ $cm^2{\cdot}s^{-1}$ for Sn [8–10], nearly 1000 times higher than that of Si and graphite [11,12]. Moreover, the Sn–Li alloy can be formed in any proportion with a much lower formation energy ($E_f$) of −0.573 eV (1 eV = $1.602176 \times 10^{-19}$ J) compared to Si and Ge (+0.401 and −0.285 eV, respectively) [13], making it widely considered to date. Among them, SnP shows a high measured capacity of 815 $mA{\cdot}h{\cdot}g^{-1}$ with the $Li^+$ diffusion channel perpendicular to the *c*-axis [14], and the resultant $Li_3P$ is also a high $Li^+$ conductor ($D_{Li^+} \approx 3 \times 10^{-3}$ $cm^2{\cdot}s^{-1}$) [15], which makes it a viable choice for ultrafast LIBs.

The lithium storage mechanism of Sn-based anode materials generally involves the first conversion reaction ($SnA_x + Li^+ + e^- \rightarrow Li_yA + Sn$) and the subsequent alloying ($Sn + Li^+ + e^- \rightarrow Li_zSn$) [16,17]. In the $Li^+$ extraction process, it has been found that the atomic level contact of $Li_xA$ and Sn can greatly improve the reversibility of the conversion reaction step, which requires a particle size of less than 10 nm [18,19]. However, high-surface-energy nanocrystals have a strong tendency to coarsen and agglomerate when cycling with fast capacity fading [20,21]. It is therefore critical to stabilize the nanocrystals in the electrochemical process. Furthermore, thermodynamic metastable SnP usually has a quite high formation energy [22,23], making controlled synthesis very difficult. Vacuum quenching and high-temperature molten salt methods are dominantly utilized to synthesize SnP with particle sizes of several hundred nanometers [24,25], resulting in extremely poor cycle stability. For example, 500 nm SnP particles give a capacity attenuation of 10% after only 40 cycles at 0.12 $A{\cdot}g^{-1}$

* Corresponding authors.
*E-mail addresses:* jianghao@ecust.edu.cn (H. Jiang), czli@ecust.edu.cn (C. Li).

https://doi.org/10.1016/j.eng.2021.11.026

[14]. Recently, nonstoichiometric $SnP_x$-based hybrids have been reported to have attractive electrochemical performance [26–29]. Typically, tens of nanometers of $Sn_4P_3$ in the carbon framework can afford more than 100 cycles, which stimulates SnP investigation [30,31]. However, a major challenge is to develop a simple and low-temperature synthesis tactic to controllably synthesize SnP with rapid electrochemical reaction kinetics.

Herein, we first demonstrate an atomic interface catalytic phosphorization strategy to confine SnP/CoP hetero-nanocrystals within reduced graphene oxide (rGO)-coated carbon cubes (denoted as TCP@C/rGO). The density functional theory (DFT) calculations disclose that the relative formation energy of SnP is significantly decreased from +0.12 to −2.05 eV when the phosphate of tin oxide is conducted on the CoP surface. More importantly, the CoP catalyst is also a conversion-type anode material with a lower lithium intercalation potential than SnP. The prior as-formed Co can accelerate the subsequent $Li^+$ insertion kinetics of SnP with rapid electron transfer, endowing it with ultrafast charge/discharge capability. A reversible capacity of 260 $mA{\cdot}h{\cdot}g^{-1}$ is achieved even at 50 $A{\cdot}g^{-1}$ (about 19 s). Furthermore, the confinement of hetero-nanocrystals within carbon frameworks effectively refrains their coarsening, exhibiting superior cycling stability almost without capacity decay (645 $mA{\cdot}h{\cdot}g^{-1}$) after 1500 cycles at 2.0 $A{\cdot}g^{-1}$.

## 2. Materials and methods

### 2.1. Synthesis of the $CoSn(OH)_6$–citrate (Cit) cubes

All reagents and solvents were of analytical grade and were used without any further purification. In the typical process, 0.35 g of $SnCl_4{\cdot}5H_2O$ (Sinopharm Chemical Reagent Beijing Co., Ltd., China), 0.238 g of $CoCl_2{\cdot}6H_2O$ (Sinopharm Chemical Reagent Beijing Co., Ltd.), and 1.56 g of sodium citrate (Sinopharm Chemical Reagent Beijing Co., Ltd.) were first dissolved in 15 mL deionized water. Then, 5 mL aqueous solution of NaOH (2 $mol{\cdot}L^{-1}$) (Shanghai Aladdin Biochemical Technology Co., Ltd., China) was added under magnetic stirring. After 1 h, 20 mL aqueous solution of NaOH (8 $mol{\cdot}L^{-1}$) was added and stirred for another 15 min. The precipitates were collected and washed with water to obtain $CoSn(OH)_6$–Cit cubes.

### 2.2. Synthesis of the TCP@C/rGO hybrids

Typically, 80 mg of the as-prepared $CoSn(OH)_6$–Cit cubes and 6.2 mg of graphene oxide (GO) were ultrasonically dispersed in 5 mL $H_2O$ with stirring for 2 h. The brown suspension was frozen in liquid nitrogen and freeze-dried to obtain the $CoSn(OH)_6$–Cit/GO precursor. Five grams of $NaH_2PO_2{\cdot}H_2O$ (Sinopharm Chemical Reagent Beijing Co., Ltd.) and 50 mg of the $CoSn(OH)_6$–Cit/GO precursor were placed at two separate positions in a tube furnace, in which $NaH_2PO_2{\cdot}H_2O$ was upstream and $CoSn(OH)_6$–Cit/GO was downstream. The TCP@C/rGO hybrids were obtained by annealing the samples at 350 °C for 30 min with a heating rate of 5 °C·$min^{-1}$ under a 100 standard cubic centimeters per minute (sccm) Ar flow.

## 3. Results and discussion

The typical design concept and fabrication route of the TCP@C/rGO hybrids is illustrated in Fig. 1. $CoSn(OH)_6$–Cit cubes are first synthesized by coprecipitating $Co^{2+}$, $Sn^{4+}$, and $OH^-$ in the presence of citrate anions. In the subsequent etching process under a high pH environment, a surface stable oxide layer can be readily generated while the as-formed $[Co(OH)_4]^{2-}$ and $[Sn(OH)_6]^{2-}$ in the core gradually dissolve, accompanied by the adsorption of citrate anions. To verify this point, a similar method was applied to synthesize pure $CoSn(OH)_6$ cubes (Fig. S1 in Appendix A) simply without adding citrates. The zeta potential is +35.5 mV, which

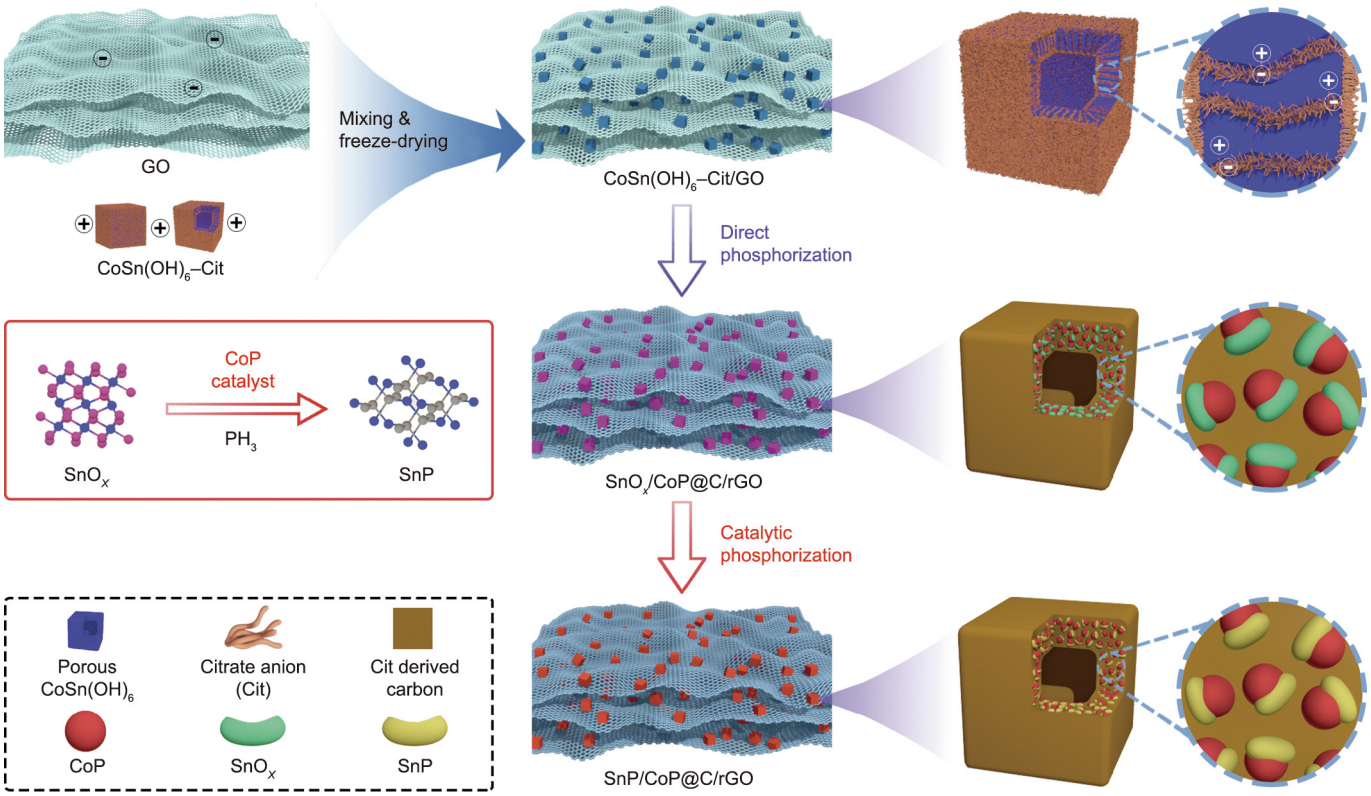


**Fig. 1.** Schematic illustration of the design and synthesis of SnP/CoP hetero-nanocrystals within rGO-coated carbon cubes by a catalytic phosphorization strategy.

decreases to +13.2 mV for the $CoSn(OH)_6$–Cit cubes, as we predicted (Fig. S2 in Appendix A). Positively charged $CoSn(OH)_6$–Cit hollow cubes are then obtained, which are easily and homogeneously dispersed on the negatively charged graphene oxide surface (−14.0 mV) with the assistance of electrostatic attraction. The traditional direct phosphorization approach easily converts Sn-based compounds into metallic Sn rather than SnP [32,33]. This fact has been further confirmed by phosphating the reported hollow $SnO_2$ spheres at 350–500 °C [34], indeed forming Sn nanoparticles with high purity (Fig. S3 in Appendix A). In this work, $CoSn(OH)_6$–Cit/GO hybrids were successfully generated into the corresponding SnP/CoP@C/rGO hybrids only at 350 °C under a $PH_3$/Ar atmosphere. The *ex-situ* X-ray diffraction (XRD) patterns and *ex-situ* Raman spectra are provided in Appendix A Fig. S4 to disclose the specific conversion process. We found that CoP is priority formed when the temperature increases to 350 °C. After retaining it from 5 to 30 min, the SnP component is gradually generated along with the disappearance of $SnO_x$. These observations indicate that CoP can catalytically phosphate Sn oxides with rapid conversion of SnP. SnP phase tin phosphide is chosen for its unique $Li^+$ diffusion channels and layered crystal structure, which make it easier to transport and store $Li^+$ than other crystal phases [14].

To further unveil the CoP-catalyzed mechanism, DFT calculations were applied to obtain the relative free energies at different reaction states during the phosphorylation of Sn oxides with and without CoP. When directly phosphating $SnO_2$ (Fig. 2(a)), we can find that metallic Sn is very easy to generate because it requires a much lower relative free energy of −2.57 eV than SnP (+0.12 eV). The specific formation pathways are illustrated in Appendix A Fig. S5. When introducing the CoP component, totally opposite phenomena are observed at the CoP/$SnO_2$ heterointerface. As shown in Fig. 2(b), CoP can dramatically reduce the energy barrier and accelerate the formation of SnP with a quite low relative free energy of −2.05 eV compared with metallic Sn (−0.22 eV). The specific formation pathways are also given in Appendix A Fig. S6. It is noted that metallic Sn has difficulty phosphate into SnP even in the presence of CoP. There were no component changes when we phosphate the mixture of CoP and

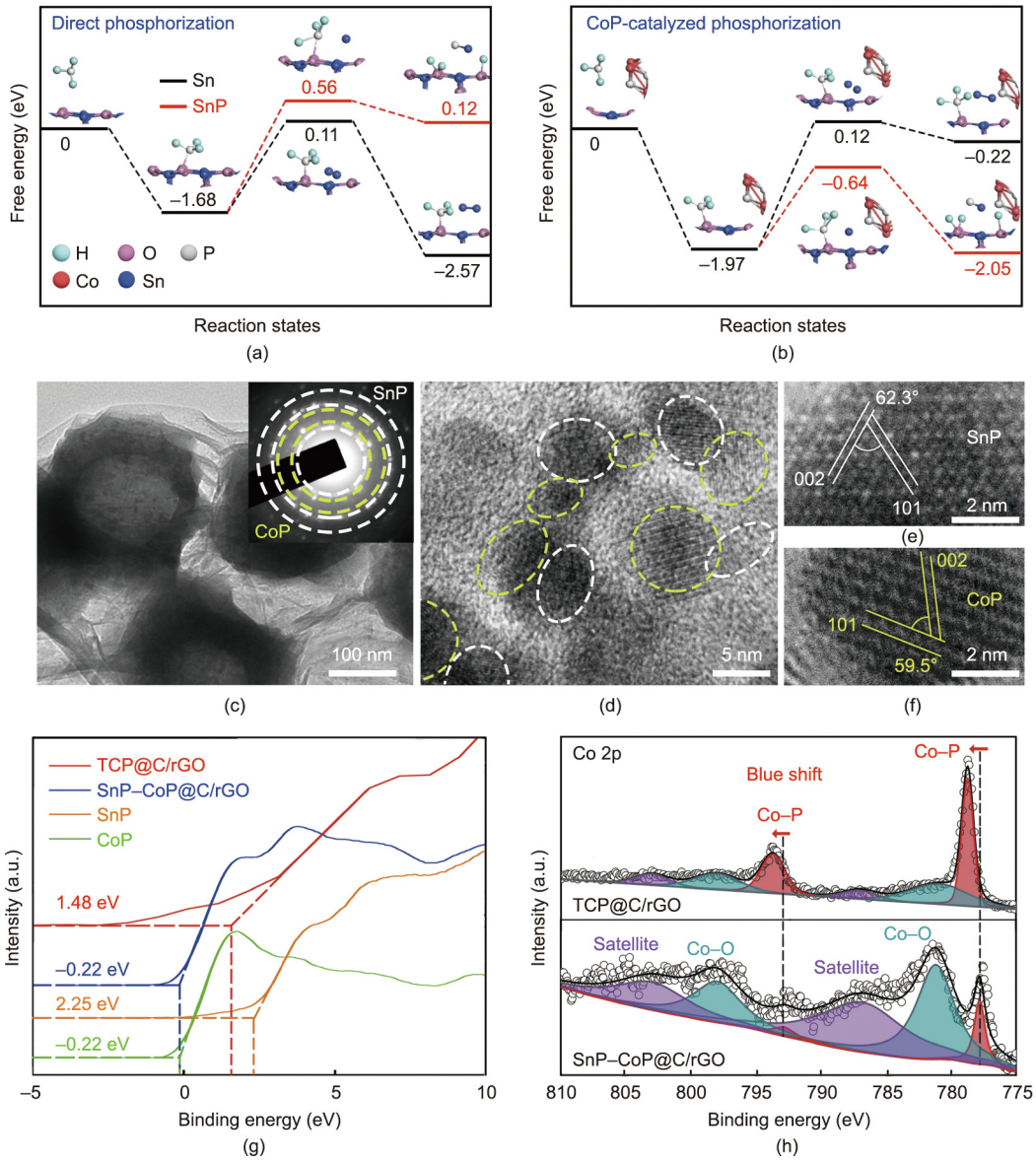


**Fig. 2.** The relative free energy versus reaction states of (a) direct phosphorization and (b) CoP-catalyzed phosphorization of $SnO_2$; (c) high-magnification (the inset showing the corresponding selected area electron diffraction (SAED) pattern); (d–f) high-resolution transmission electron microscope (TEM) images of the TCP@C/rGO hybrids; (g) VB-XPS spectra; (h) XPS Co 2p spectra of the samples.

Sn nanoparticles under similar conditions (Fig. S7 in Appendix A). These observations are highly consistent with the aforementioned experimental results.

The detailed structural characterizations of the TCP@C/rGO hybrids are shown in Fig. 2(c). Hollow TCP@C cubes with lengths of about 200 nm are well covered by rGO nanosheets. The same observation is also obtained in the low-magnification scanning electron microscope (SEM; S-4800, Hitachi Ltd., Japan) image (Fig. S8 in Appendix A). We can only see the SnP and CoP electron diffraction patterns in the corresponding inset. Further magnifying the wall of the TCP@C cubes, we can observe the SnP/CoP hetero-nanocrystals in Fig. 2(d) due to the CoP-catalyzed phosphorization strategy, which are embedded into citrate-derived carbon. The typical staggered arrangement of the SnP and CoP nanocrystals indicates that CoP can effectively prevent the migration and agglomeration of Sn during the electrochemical process. Both of them are marked with white (SnP) and yellow (CoP) dashed circles, respectively. Lattice distances of 0.30 and 0.32 nm are assigned to the (002) and (011) planes of SnP in Fig. 2(e), while 0.38 and 0.28 nm are the (101) and (002) planes of CoP in Fig. 2(f). The SnP/CoP heterostructure features are also verified by valance-band X-ray photoelectron spectroscopy (VB-XPS; AXIS Ultra DLD, Kratos Empire Ltd., China), as shown in Fig. 2(g). The as-obtained TCP@C/rGO hybrids give a valence-band maximum (VBM) value of 1.48 eV, between −0.22 eV for pure CoP and 2.25 eV for pure SnP because of the valence band curvature. The SnP–CoP@C/rGO hybrids show VBM values of −0.22 eV because hetero-nanocrystals are not formed. A similar phenomenon can also be observed in their ultraviolet–visible (UV–vis; UV-2600, Shimadzu Co., Japan) spectra (Fig. S9 in Appendix A), indicating a strong interaction between them. An in-depth analysis of the electronic structure was implemented by XPS (AXIS Ultra DLD). The Co 2p spectra in Fig. 2(h) show that an obvious blueshift of about 0.8 eV for Co–P peaks can be observed in the TCP@C/rGO hybrids compared to the SnP/CoP@C/rGO hybrids, indicating the formation of Co–P–Sn bonds at the hetero-nanocrystal interfaces [35]. The corresponding P 2p spectra further verify this point (Fig. S10 in Appendix A). A detailed discussion is provided in the Appendix A.

The atomic ratio of Sn, Co, and P is 1:1:2 for the TCP@C/rGO hybrids with a weight ratio of 79.7% based on the inductively coupled plasma mass spectrometry (ICP–MS ELAN DRC-e, PerkinElmer, Inc., USA) results. We then completely removed the SnP/CoP hetero-nanocrystals by acid etching. As shown in Appendix A Fig. S11, many mesopores are left in the resultant carbon frameworks, and a strong peak at 4.0 nm appears in the pore size distribution curve, further clarifying the embedded nanostructures and indicating that the grain coarsening of the nanocrystals during charge/discharge cycles can be effectively inhibited. Based on the above discussion, Fig. S12 in Appendix A shows the formation schematic illustration of SnP for direct phosphorization and CoP-catalyzed phosphorization of $SnO_2$. The interface-catalyzed phosphorization at the atomic level determines the total conversion of $SnO_2$ into SnP. If phosphorization occurs at the particle level, the main component is metallic Sn with few SnP in their interface, which is confirmed in the experiment (Fig. S13 in Appendix A).

Analogous hybrids with SnP/CoP hetero-nanocrystals sized about 20 and 50 nm were also synthesized as controls just by reannealing the TCP@C/rGO hybrids for the prescribed time, denoted TCP-1@C/rGO and TCP-2@C/rGO, respectively (Fig. S14 in Appendix A). The three samples are evaluated by charge–discharge measurements. The initial coulombic efficiency of the TCP@C/rGO hybrids was 74.1%. The average reversible capacities for five cycles at 0.5 $A{\cdot}g^{-1}$ are illustrated in Fig. 3(a). The capacity shows rapid attenuation as the size of the SnP nanoparticles increases. The targeted TCP@C/rGO hybrids show the highest capacity of 907 $mA{\cdot}h{\cdot}g^{-1}$ at 0.5 $A{\cdot}g^{-1}$ compared to the two controls. More impressively, it possesses ultrafast charge–discharge capability and ultrastable cycle performance. Even at 50 $A{\cdot}g^{-1}$ (charging for 19 s), 260 $mA{\cdot}h{\cdot}g^{-1}$ is still retained. After 1500 continuous cycles at 2.0 $A{\cdot}g^{-1}$, the capacity is always 645 $mA{\cdot}h{\cdot}g^{-1}$ without degradation, as shown in Fig. 3(b). Nevertheless, the TCP-1@C/rGO hybrids show a rapid capacity fading from 522 to 247 $mA{\cdot}h{\cdot}g^{-1}$ only after 300 cycles. The TCP-2@C/rGO hybrids exhibit a 21.1% capacitance retention only after 200 cycles with poor reversibility, which is unnecessary in the latter discussion. The rate and cycling performances imply that the SnP particle size has significant effects on the lithium storage ability. Our TCP@C/rGO hybrids can also achieve 82% capacity retention after 500 cycles, even at 10.0 $A{\cdot}g^{-1}$ (Fig. S15 in Appendix A). Such superior lithium storage performances have been compared with some typical Sn-based anode materials by choosing several key indices, including reversible specific capacity,

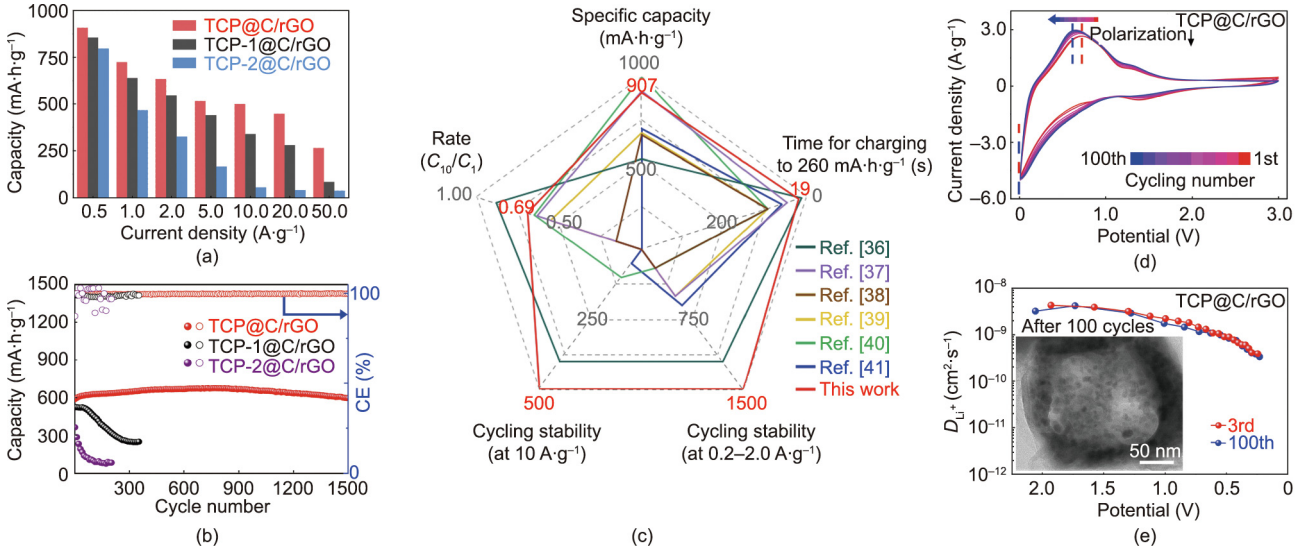


**Fig. 3.** (a) The reversible specific capacity at 0.5–50.0 $A{\cdot}g^{-1}$ and (b) cycling stability at 2.0 $A{\cdot}g^{-1}$ of the targeted TCP@C/rGO hybrids with different SnP/CoP sizes; (c) comprehensive comparison of the reported Sn-based anode materials with the targeted TCP@C/rGO hybrids; (d) cyclic voltammetry (CV) curves at 3.0 $mV{\cdot}s^{-1}$ from the 1st to 100th cycle; (e) galvanostatic intermittent titration technique (GITT) curves of the targeted TCP@C/rGO hybrids before and after 100 cycles (inset showing the TEM image after 100 cycles). CE: coulombic efficiency; $C_{10}$: capacity at 10 $A{\cdot}g^{-1}$; $C_1$: capacity at 1 $A{\cdot}g^{-1}$.

charging/discharging rates and cycle life at various current densities [36–41], as shown in Fig. 3(c). The targeted TCP@C/rGO hybrids exhibit obviously enhanced LIB performance.

Fig. 3(d) shows the cyclic voltammetry (CV) curves of the TCP@C/rGO hybrids during 100 cycles at 3.0 $mV{\cdot}s^{-1}$. The well-overlapped CV curves and the slight shift of the redox peak to low potential imply a gradually decreased electrochemical polarization and high charging/discharging reversibility. In contrast, the redox peak decreases obviously for the TCP-1@C/rGO hybrids during 100 cycles (Fig. S16 in Appendix A), indicating relatively poor reversibility when increasing the SnP/CoP nanoparticles to 20 nm. The electrochemical impedance spectroscopies (EISs) of the above two samples at the 3rd, 50th, and 100th cycles are also provided in Fig. S17 and Table S1 in Appendix A. The charge transfer resistance ($R_{ct}$) of the TCP@C/rGO hybrids decreases from 21.7 to 5.2 Ω, while the TCP-1@C/rGO hybrids show an increase from 95.7 to 205.6 Ω after 100 cycles. Furthermore, the $Li^+$ diffusion coefficient ($D_{Li^+}$) of the TCP@C/rGO hybrids reaches $5.0 \times 10^{-9}$ $cm^2{\cdot}s^{-1}$, which is almost constant before and after 100 cycles, as shown in Fig. 3(e). The corresponding inset gives the transmission electron microscope (TEM) image after cycling. The about 4 nm SnP/CoP particles are maintained and well distributed in the carbon framework. In the TCP-1@C/rGO hybrids with about 20 nm SnP/CoP particles, the value of $D_{Li^+}$ is only $1.0 \times 10^{-9}$ $cm^2{\cdot}s^{-1}$ at the 3rd cycle and $10^{-11}$ $cm^2{\cdot}s^{-1}$ at the 100th cycle (Fig. S18 in Appendix A). These results suggest that the particle size has significant effects on the electrochemical performance, which are further verified by studying the lithium storage behaviors of the two samples after the 3rd and 100th cycles. As shown in Appendix A Fig. S19, the capacitive dominated contribution of the TCP@C/rGO hybrids gives a slight decrease from 76.8% at the 3rd cycle to 69.7% at the 100th cycle. However, the TCP-1@C/rGO hybrids exhibit a sharp drop of 40% after 100 cycles. This analysis indicates that the ultrasmall SnP/CoP nanocrystals contribute much more capacitive capacity, therefore endowing a high specific capacity even at ultrafast charge/discharge rates and superior cycling stability.

Fig. 4(a) provides the initial three CV curves of the targeted TCP@C/rGO hybrids at 0.2 $mV{\cdot}s^{-1}$ within 0.01–3.00 V. In the first lithiation process, the peak at 1.5 V is assigned to the conversion of CoP and SnP into the corresponding metal as well as the formation of the solid electrolyte interface (SEI) layer, and the peak at 0.01 V belongs to the alloying of Sn into $Li_xSn$. The following charge and discharge curves highly overlap. The redox reactions of CoP occur in the red area, where the peaks at 1.8 and 2.5 V correspond to the reversible conversion reactions of CoP + $x$Li ↔ Co + $Li_xP$. The next yellow area is the SnP lithiation and delithiation process. It also shows high reversibility due to the conversion into metallic Co of CoP, which further accelerates the electron transfer during lithiation, as shown in the schematic of the inset. In contrast, the CV curves of the TCP-1@C/rGO hybrids decrease obviously without the redox peaks of CoP reversible reactions, as shown in Fig. 4(b). These phenomena imply that the crystal size has significant effects on the lithiation reactions. To further clarify their reaction mechanism, the discharge/charge profiles and the corresponding *ex-situ* XPS results of the TCP@C/rGO hybrids are provided in Appendix A Fig. S20. The electrochemical process of the TCP@C/rGO hybrids is summarized as CoP + $x$$Li^+$ + $xe^-$ ↔ Co + $Li_xP$, SnP + $y$$Li^+$ + $ye^-$ ↔ Sn + $Li_yP$, and Sn + $z$$Li^+$ + $ze^-$ ↔ $Li_zSn$. Specifically, in the first discharge process, the Co–P and Sn–P peaks totally disappear at 1.0 V along with the appearance of the corresponding $Co^0$ and $Sn^0$ peaks. After further discharging to 0.01 V, the peak of $Sn^0$ shifts to a higher binding energy of Sn–Li. In the following charge process, the peak of Sn–Li disappears with the appearance of $Sn^0$ at 0.8 V, which then fully turns into the Sn–P bond at 1.7 V. When charging to 3.0 V, the Co–P bonds reappear without the $Co^0$ peak. In the second discharge process, the chemical bond change is almost the same as that in the first discharge process, indicating high electrochemical reversibility. The coupling effects among them are further verified by the reaction resistance calculated by the galvanostatic intermittent titration technique (GITT) results during the discharge process (Fig. S21 in Appendix A) [42,43]. The TCP@C/rGO hybrids exhibit two obvious decreased reaction resistances at about 2.0 and 0.6 V, assigned to the generation of Co and Sn, respectively. By comparison, the TCP-1@C/rGO hybrids show only one reduced reaction resistance at about 0.6 V, agreeing with the aforementioned observations. Fig. S22 and Table S2 in Appendix A give the EIS curves when discharging from 3.0 to 1.0 V. The $R_{ct}$ of the TCP@C/rGO electrode is significantly reduced from 21.7 to 8.3 Ω, also indicating the greatly enhanced charge transfer enabled by the generated metallic Co.

Electric field finite element simulations are applied to extensively analyze the current density distributions on different crystal sizes of the heterostructured nanocrystals within rGO-coated carbon cube hybrids. A circuit is first built, and the two dimensional (2D) section model of the SnP/CoP hetero-nanocrystals distribution is also given in Fig. 4(c). The relative current density distributions of the 4 and 20 nm SnP/CoP heterocrystals in the carbon frameworks are shown in Fig. 4(d). The current density of the conductive carbon is approximately 1000 times higher than that of the SnP/CoP heterocrystals, hence showing blue for SnP/CoP in low-magnification mapping. After magnification, almost the same current distribution can be observed for SnP and CoP, chiefly due to their similar resistance values. Obviously, the current density of the crystals with sizes of 4 nm is much higher than that of the corresponding 20 nm crystals. We also simulated the current density distributions of crystals of other sizes (Fig. S23 in Appendix A), and the average current density values at the crystal centers ($J_c$) are shown in Fig. 4(e). A linear relationship is built when the crystal sizes are in the range of 4–20 nm. However, there is no large current change (< 4%) even for 2 nm crystals. The dynamic relative current density distributions were further investigated under 1.0 V based on the conversion degree ($D_c$) of CoP into Co during the discharging process (Fig. S24 in Appendix A). Fig. 4(f) gives the current density distributions of the initial ($D_c$ = 0) and final states ($D_c$ = 100%) for SnP crystals, indicating that the full conversion of CoP can remarkably increase the current density. The coefficient of variation ($\delta$) is then introduced to evaluate the uniformity of the current density distribution. The relationship of the average current density in SnP crystals ($J_a$) and $\delta$ with $D_c$ is provided in Fig. 4(g). As $D_c$ increases from 0 to 100%, the value of $J_a$ increases by 4.4 times from 52 to 229 $A{\cdot}cm^{-2}$. In the process of dynamic conversion of CoP into Co with $D_c$ = 25%–87%, the $J_a$ value of SnP adjacent to Co always reaches 200 $A{\cdot}cm^{-2}$, while there is almost no change for SnP adjacent to CoP, which results in a relatively high $\delta$ value. This value then drops to 47.6% with $D_c$ = 100%, indicating that the high reversibility of CoP conversion is good at improving the current distribution in SnP. These results are highly consistent with the above experimental results and related analysis.

## 4. Conclusions

In summary, this work demonstrates a low-temperature CoP-catalytic phosphorization strategy for confining SnP/CoP hetero-nanocrystals within rGO-coated carbon frameworks as anode materials for ultrafast LIBs with superior cycling stability (645 $mA{\cdot}h{\cdot}g^{-1}$ after 1500 cycles at 2 $A{\cdot}g^{-1}$) and ultrahigh rate capability (260 $mA{\cdot}h{\cdot}g^{-1}$ at 50 $A{\cdot}g^{-1}$). The DFT calculations disclose that the relative formation energy of SnP is significantly decreased when tin oxide is phosphorylated on the CoP surface. The *ex-situ*

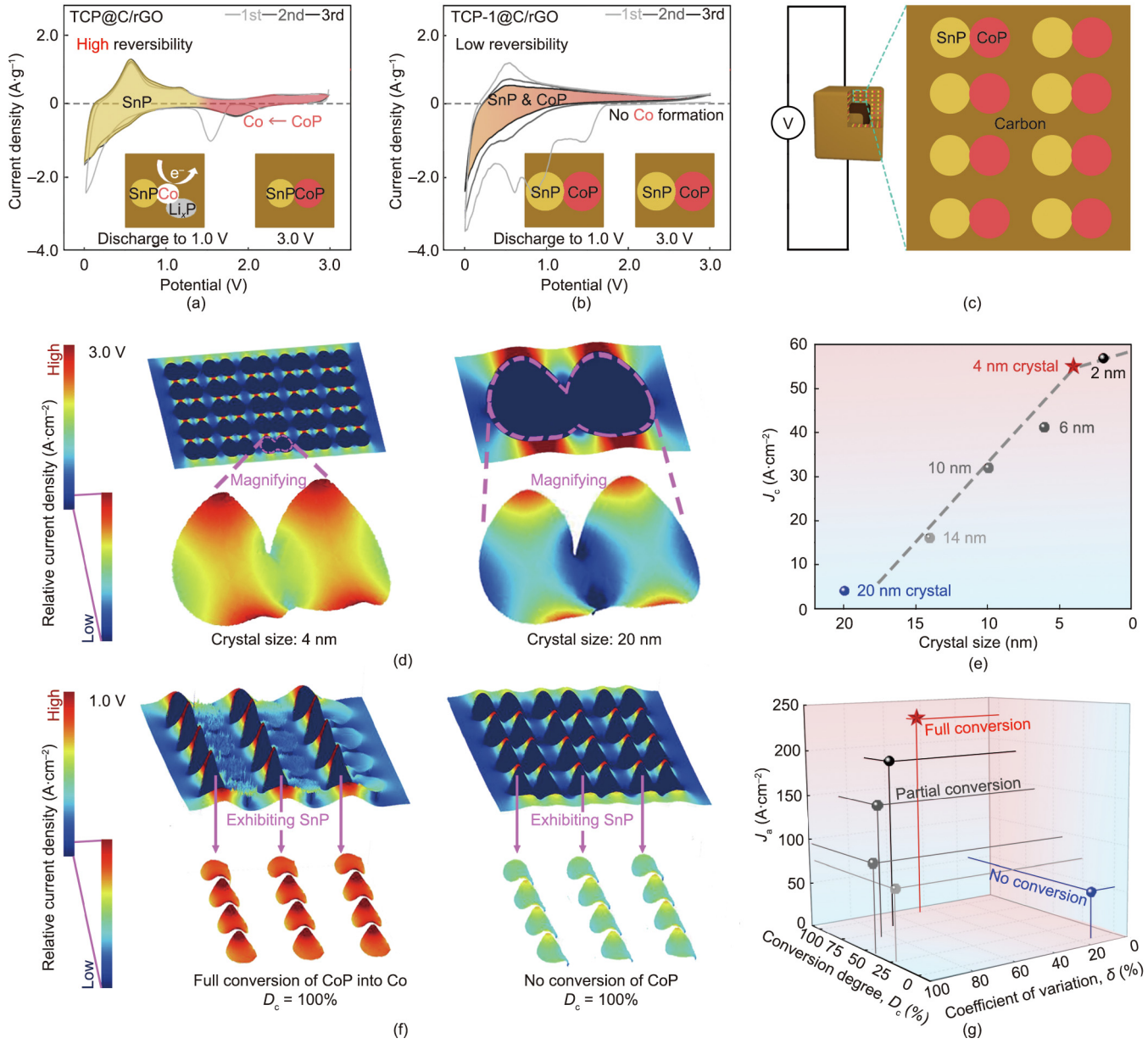


**Fig. 4.** The initial three CV curves at 0.2 mV·s$^{-1}$ of (a) the TCP@C/rGO hybrids and (b) the TCP-1@C/rGO hybrids; (c) schematic of a TCP@C cube in circuit and its 2D section for finite element simulation; (d) the relative current density distribution and (e) the average current density at crystal centers of the simulated models with different crystal sizes; (f) the relative current density distribution and (g) the average current density and the coefficient of variation in SnP crystals of the simulated models with different CoP conversion degrees.

XPS analysis and CV curves clarify the lithiation/delithiation mechanism, discovering that the electrochemical reversibility of SnP/CoP hetero-nanocrystals is closely related to their sizes (< 4 nm) and that the previously formed metallic Co of conversion-type CoP at relatively high potential can further accelerate the subsequent $Li^+$ insertion kinetics of SnP, hence endowing it with ultrafast charge/discharge performances. The dynamic relative current density distributions of SnP have been further investigated by finite element analysis, indicating that the current density remarkably increases with the $D_c$ of CoP into metallic Co. This finding offers deep insights to stimulate the rapid developments in Sn-based anode materials for ultrafast LIBs.

## Acknowledgments

This work was supported by the National Natural Science Foundation of China (21975074, 21838003, and 91834301), the Social Development Program of Shanghai (17DZ1200900), the Shanghai Scientific and Technological Innovation Project (18JC1410500), and the Fundamental Research Funds for the Central Universities (222201718002).

## Compliance with ethics guidelines

Chen Hu, Yanjie Hu, Aiping Chen, Xuezhi Duan, Hao Jiang, and Chunzhong Li declare that they have no conflict of interest or financial conflicts to disclose.

## Appendix A. Supplementary data

Supplementary data to this article can be found online at https://doi.org/10.1016/j.eng.2021.11.026.

## References


[1] Liu Y, Zhu Y, Cui Y. Challenges and opportunities towards fast-charging battery materials. Nat Energy 2019;4(7):540–50.
[2] Zhao W. A forum on batteries: from lithium-ion to the next generation. Natl Sci Rev 2020;7(7):1263–8.
[3] Babu B, Simon P, Balducci A. Fast charging materials for high power applications. Adv Energy Mater 2020;10(29):2001128.
[4] Choi S, Kwon TW, Coskun A, Choi JW. Highly elastic binders integrating polyrotaxanes for silicon microparticle anodes in lithium ion batteries. Science 2017;357(6348):279–83.
[5] Liu T, Chu Q, Yan C, Zhang S, Lin Z, Lu J. Interweaving 3D network binder for high-areal-capacity Si anode through combined hard and soft polymers. Adv Energy Mater 2019;9(3):1802645.
[6] Jin H, Wang H, Qi Z, Bin DS, Zhang T, Wan Y, et al. A black phosphorus-graphite composite anode for Li-/Na-/K-ion batteries. Angew Chem Int Ed Engl 2020;59(6):2318–22.
[7] Wu Y, Wang W, Ming J, Li M, Xie L, He X, et al. An exploration of new energy storage system: high energy density, high safety, and fast charging lithium ion battery. Adv Funct Mater 2019;29(1):1805978.
[8] Genser O, Hafner J. Structure and bonding in crystalline and molten Li–Sn alloys: a first-principles density-functional study. Phys Rev B 2001;63(14):144204.
[9] Wen CJ, Huggins RA. Chemical diffusion in intermediate phases in the lithium–tin system. J Solid State Chem 1980;35(3):376–84.
[10] Shi J, Wang Z, Fu YQ. Density functional theory study of diffusion of lithium in Li–Sn alloys. J Mater Sci 2016;51(6):3271–6.
[11] Fedorov AS, Kuzubov AA, Eliseeva NS, Popov ZI, Visotin MA, Galkin NG. Theoretical study of the lithium diffusion in the crystalline and amorphous silicon as well as on its surface. Solid State Phenom 2014;213:29–34.
[12] Levi MD, Aurbach D. Diffusion coefficients of lithium ions during intercalation into graphite derived from the simultaneous measurements and modeling of electrochemical impedance and potentiostatic intermittent titration characteristics of thin graphite electrodes. J Phys Chem B 1997;101(23):4641–7.
[13] Chou CY, Kim H, Hwang GS. A comparative first-principles study of the structure, energetics, and properties of Li–M (M = Si, Ge, Sn) alloys. J Phys Chem C 2011;115(40):20018–26.
[14] Kim Y, Hwang H, Yoon CS, Kim MG, Cho J. Reversible lithium intercalation in teardrop-shaped ultrafine $SnP_{0.94}$ particles: an anode material for lithium-ion batteries. Adv Mater 2007;19(1):92–6.
[15] Nazri G. Preparation, structure and ionic conductivity of lithium phosphide. Solid State Ion 1989;34(1–2):97–102.
[16] Park MG, Lee DH, Jung H, Choi JH, Park CM. Sn-based nanocomposite for Li-ion battery anode with high energy density, rate capability, and reversibility. ACS Nano 2018;12(3):2955–67.
[17] Liang SZ, Cheng YJ, Zhu J, Xia YG, Müller-Buschbaum P. A chronicle review of nonsilicon (Sn, Sb, Ge)-based lithium/sodium-ion battery alloying anodes. Small Methods 2020;4(8):2000218.
[18] Hu R, Chen D, Waller G, Ouyang Y, Chen Yu, Zhao B, et al. Dramatically enhanced reversibility of $Li_2O$ in $SnO_2$-based electrodes: the effect of nanostructure on high initial reversible capacity. Energy Environ Sci 2016;9(2):595–603.
[19] Xia Y, Han S, Zhu Y, Liang Y, Gu M. Stable cycling of mesoporous $Sn_4P_3/SnO_2$@C nanosphere anode with high initial coulombic efficiency for Li-ion batteries. Energy Storage Mater 2019;18:125–32.
[20] Wang J, Huang W, Kim YS, Jeong YK, Kim SC, Heo J, et al. Scalable synthesis of nanoporous silicon microparticles for highly cyclable lithium-ion batteries. Nano Res 2020;13(6):1558–63.
[21] Ying H, Han WQ. Metallic Sn-based anode materials: application in high-performance lithium-ion and sodium-ion batteries. Adv Sci 2017;4(11):1700298.
[22] Gullman J. The crystal structure of SnP. J Solid State Chem 1990;87(1):202–7.
[23] Ritscher A, Schmetterer C, Ipser H. Pressure dependence of the tin–phosphorus phase diagram. Monatsh Chem 2012;143(12):1593–602.
[24] Katz G, Kohn JA, Broder JD. Crystallographic data for tin monophosphide. Acta Crystallogr 1957;10(9):607.
[25] Aso K, Kitaura H, Hayashi A, Tatsumisago M. $SnP_{0.94}$ active material synthesized in high-boiling solvents for all-solid-state lithium batteries. J Ceram Soc Jpn 2010;118(1379):620–62.
[26] Liu J, Kopold P, Wu C, van Aken PA, Maier J, Yu Y. Uniform yolk-shell $Sn_4P_3$@C nanospheres as high-capacity and cycle-stable anode materials for sodium-ion batteries. Energy Environ Sci 2015;8(12):3531–8.
[27] Wang W, Zhang J, Yu DYW, Li Q. Improving the cycling stability of $Sn_4P_3$ anode for sodium-ion battery. J Power Sources 2017;364:420–45.
[28] Xu Y, Peng B, Mulder FM. A high-rate and ultrastable sodium ion anode based on a novel $Sn_4P_3$–P@Graphene nanocomposite. Adv Energy Mater 2018;8(3):1701847.
[29] Choi J, Kim WS, Kim KH, Hong SH. $Sn_4P_3$–C nanospheres as high capacitive and ultra-stable anodes for sodium ion and lithium ion batteries. J Mater Chem A 2018;6(36):17437–43.
[30] Ding Y, Li ZF, Timofeeva EV, Segre CU. *In situ* EXAFS-derived mechanism of highly reversible tin phosphide/graphite composite anode for Li-ion batteries. Adv Energy Mater 2018;8(9):1702134.
[31] Fan X, Gao T, Luo C, Wang F, Hu J, Wang C. Superior reversible tin phosphide-carbon spheres for sodium ion battery anode. Nano Energy 2017;38:350–7.
[32] Wang A, Qin M, Guan J, Wang L, Guo H, Li X, et al. The synthesis of metal phosphides: reduction of oxide precursors in a hydrogen plasma. Angew Chem Int Ed Engl 2008;47(32):6052–4.
[33] Yang Y, Zhao X, Wang H, Li M, Hao C, Ji M, et al. Phosphorized $SnO_2$/graphene heterostructures for highly reversible lithium-ion storage with enhanced pseudocapacitance. J Mater Chem A 2018;6(8):3479–87.
[34] Lou XW, Wang Y, Yuan C, Lee JY, Archer LA. Template-free synthesis of $SnO_2$ hollow nanostructures with high lithium storage capacity. Adv Mater 2006;18(17):2325–9.
[35] Li H, Zhu Y, Zhao K, Fu Q, Wang K, Wang Y, et al. Surface modification of coordination polymers to enable the construction of CoP/N, P-codoped carbon nanowires towards high-performance lithium storage. J Colloid Interface Sci 2020;565:503–12.
[36] Jiang Y, Li Y, Zhou P, Lan Z, Lu Y, Wu C, et al. Ultrafast, highly reversible, and cycle-stable lithium storage boosted by pseudocapacitance in Sn-based alloying anodes. Adv Mater 2017;29(48):1606499.
[37] Mo R, Tan X, Li F, Tao R, Xu J, Kong D, et al. Tin–graphene tubes as anodes for lithium-ion batteries with high volumetric and gravimetric energy densities. Nat Commun 2020;11(1):1374.
[38] Zhou X, Dai Z, Liu S, Bao J, Guo YG. Ultra-uniform $SnO_x$/carbon nanohybrids toward advanced lithium-ion battery anodes. Adv Mater 2014;26(23):3943–9.
[39] Wu C, Maier J, Yu Y. Sn-based nanoparticles encapsulated in a porous 3D graphene network: advanced anodes for high-rate and long life Li-ion batteries. Adv Funct Mater 2015;25(23):3488–96.
[40] Ferrara G, Arbizzani C, Damen L, Guidotti M, Lazzari M, Vergottini FG, et al. High-performing Sn–Co nanowire electrodes as anodes for lithium-ion batteries. J Power Sources 2012;211:103–7.
[41] Ke FS, Huang L, Jamison L, Xue LJ, Wei GZ, Li JT, et al. Nanoscale tin-based intermetallic electrodes encapsulated in microporous copper substrate as the negative electrode with a high rate capacity and a long cycle ability for lithium-ion batteries. Nano Energy 2013;2(5):595–603.
[42] Yang Y, Qu X, Zhang X, Liu Y, Hu J, Chen J, et al. Higher than 90% initial coulombic efficiency with staghorn-coral-like 3D porous $LiFeO_{2-x}$ as anode materials for Li-ion batteries. Adv Mater 2020;32(22):1908285.
[43] Xu Y, Zhu Y, Liu Y, Wang C. Electrochemical performance of porous carbon/tin composite anodes for sodium-ion and lithium-ion batteries. Adv Energy Mater 2013;3(1):128–33.